# DECREASE OF APPARENT TENSILE AND BENDING STRENGTH WITH SPECIMEN SIZE: TWO DIFFERENT EXPLANATIONS BASED ON FRACTURE MECHANICS

ALBERTO CARPINTERI

Department of Structural Engineering, Politecnico di Torino, 10129 Torino, Italy

**Abstract**—The influence of the shape and size distribution of defects on material strength is investigated. Constant reference is made to Weibull Theory and Fracture Mechanics, and a family of regular polygonal voids is considered with the two limit-cases of Griffith cracks and circular pores. A defect size distribution of proportionality is defined, for which the maximum defect size turns out to be proportional to the linear size of the body. In this way, a very general analytical expression for the *tensile strength* decrease with size is obtained and then confirmed by experimental evidence.

Specimen size is also shown to have a fundamental influence on global structural behaviour, which can range from ductile to brittle when strain softening and strain localization are taken into account. The brittle behaviour coincides with a snap-back instability in the load–deflection path, which shows a positive slope in the softening branch. Such a virtual branch may be revealed only if the loading process is controlled by a monotonically increasing function of time (e.g. the crack opening displacement). Otherwise, the loading capacity will present a discontinuity with a negative jump.

A general explanation of the well-known decrease in *bending strength* by increasing the specimen sizes is given in terms of dimensional analysis. Due to the different physical dimensions of strength $[FL^{-2}]$ and toughness $[FL^{-1}]$, the true value of such material property may be found exactly only with comparatively large specimens.

## 1. INTRODUCTION

It is a matter of fact that the strength of structural materials is not constant—it decreases with increasing size of the specimen. Such a phenomenon was analyzed by Weibull (1939) nearly fifty years ago through the application of the "weakest link concept". It consists in the hypothesis that the probability of finding a critical imperfection in a given material increases with increasing volume. This is a simple assumption which does not describe either the nature of the imperfections or the constitutive law of the material. More recently, Freudenthal (1968) and Jayatilaka (1979) considered a linear-elastic material with a great number of embedded Griffith cracks. They proved that the variability of tensile strength with specimen volume may be connected with the probability density of crack size distribution.

Several materials used in civil engineering, for example concrete, rocks and fiber-reinforced cement composites, present softening in their ultimate behaviour under loading (Bazant, 1976). The size-scale of the specimen has often revealed a fundamental influence on the global structural behaviour. Whereas in elasticity and plasticity, geometrically similar structures behave in the same way, when strain-softening and strain-localization are taken into account, the structural behaviour ranges from ductile to brittle merely by increasing the size, and keeping material properties and geometrical shape unchanged. In classical plasticity, only energy dissipation per unit volume is allowed, whereas, if energy dissipation per unit area is also contemplated, the global brittleness becomes scale-dependent.

The influence of the shape and size distributions of the defects on the tensile strength is investigated in Sections 2 and 3 respectively. A family of regular polygonal voids is considered with the two limit-cases of Griffith cracks and circular pores. A general explanation is thus obtained for the *tensile strength* decrease with size (from the true value down to zero) and then confirmed by experimental evidence.

Limit analyses for slabs in tension and beams in flexure are proposed in Sections 4 and 5 respectively, assuming cohesive forces between the two opposite crack surfaces. Such a simple approach shows a clear trend towards brittle behaviour for large size. When the softening load–deflection branch presents positive slope, a snap-back instability occurs

(Maier, 1968). If the loading process is displacement-controlled, the loading capacity will present a discontinuity with a negative jump. Such results are confirmed by a more refined finite element investigation in Section 6. The *bending strength* appears to decrease with size from three times the true value down to the true value for infinite size. A cohesive crack model is utilized to analyze slow crack growth in bending. Such a model was introduced by Barenblatt (1959), and then applied with some modifications by several authors : Dugdale (1960), Bilby *et al.* (1963), Rice (1968), Hillerborg *et al.* (1976) and others.

Tensile strength and bending strength both turn out to be decreasing functions of size. On the other hand, such functions appear different and produced by substantially different causes.

## 2. STRUCTURES WITH A DOMINANT DEFECT

Let us consider a two-dimensional linear-elastic structure with an edge Griffith crack (Fig. 1(a)). Referring to the well-known paper by Irwin (1957), the symmetrical stress field around the crack tip can be described by the following expression :
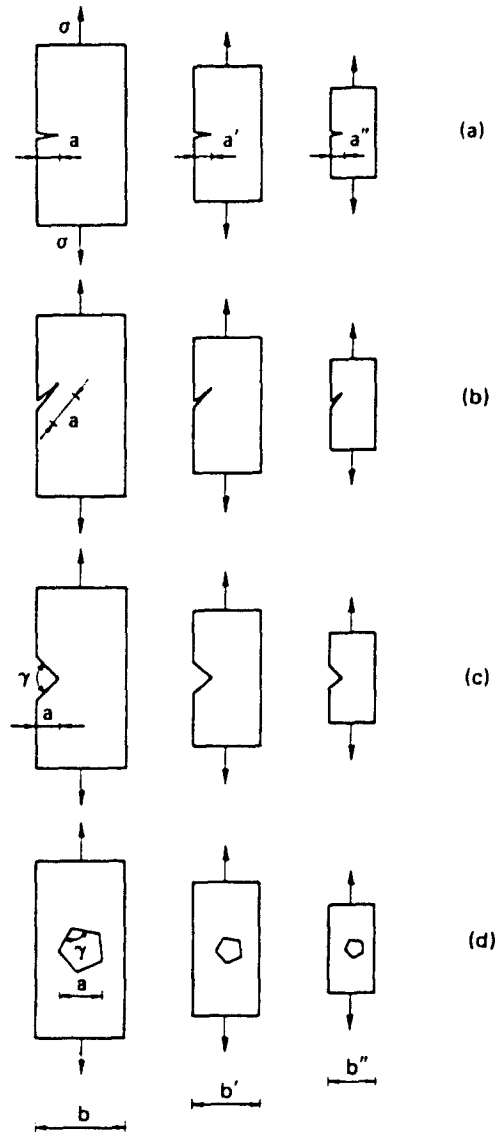


Fig. 1. Geometrically similar structures with a dominant defect : (a) opening crack ; (b) mixed mode crack ; (c) re-entrant corner ; (d) polygonal void.

$$\sigma_{ij} = Kr^{-1/2}S_{ij}(\vartheta),$$ (1)

where $K$ is the amplification factor of the stress-singularity (stress-intensity factor) and $r$ and $\vartheta$ are the radial and angular coordinates respectively.

For every geometrical shape of the structure, it is possible to express the $K$-factor by

$$K = \sigma b^{1/2}f(a/b),$$ (2)

where $\sigma$ is the nominal stress, $b$ is a characteristic size of the structure and $f$ is a shape-factor depending on the geometry of structure and on the ratio of crack length $a$ to reference size $b$ (Sih, 1973).

The stress of failure $\sigma_f$ is reached when the $K$-factor is equal to its critical value $K_c$:

$$\sigma_f = K_c b^{-1/2}\frac{1}{f(a/b)}.$$ (3)

If the logarithms of both sides of eqn (3) are considered, we obtain:

$$\ln \sigma_f = [\ln K_c - \ln f(a/b)] - \tfrac{1}{2}\ln b,$$ (4)
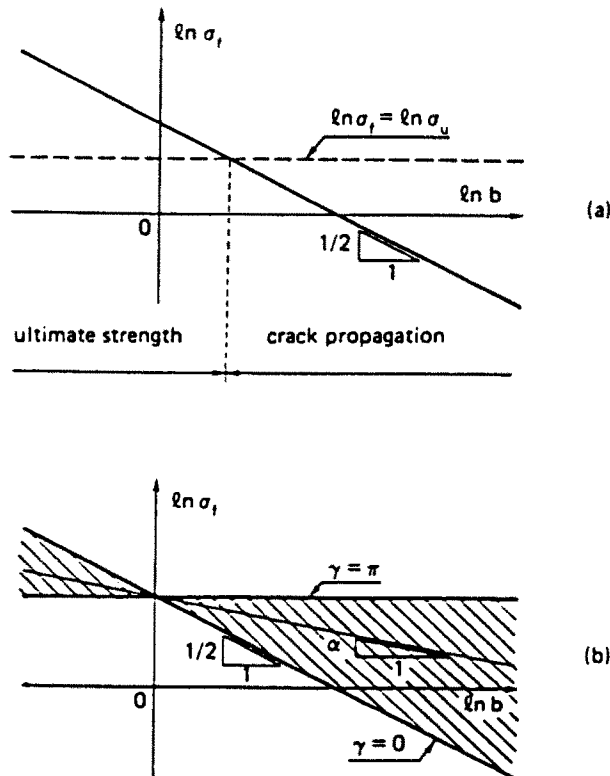
or, more concisely,



Fig. 2. Bi-logarithmic strength vs size graph: (a) interaction between ultimate strength collapse and crack propagation; (b) attenuation of the strength decrease when the re-entrant corner angle increases.

$$\ln \sigma_f = A\left(K_c, \frac{a}{b}\right) - \tfrac{1}{2} \ln b, \tag{5}$$

where function $A$ depends on the shape of structure, as well as on material and crack depth.

If we keep the material and the structural shape constant and take into consideration a set of geometrically similar structures (Fig. 1(a)), the strength $\ln \sigma_f$ will turn out to be a linearly decreasing function, with slope $-1/2$, of the scale-parameter $\ln b$ (Fig. 2(a)).

If the material presents an intrinsic strength $\sigma_u$, the horizontal line

$$\ln \sigma_f = \ln \sigma_u \tag{6}$$

will limit the strength for $b \to 0^+$ in Fig. 2(a). In fact, as already observed by Walsh (1972) and Carpinteri (1982a, b), when the structural size is relatively small, the ultimate strength failure precedes the crack propagation.

When the Griffith crack is subjected to a mixed mode loading (Fig. 1(b)), the stress field at the crack tip is

$$\sigma_{ij} = \sum_{v=1}^{2} K_v r^{-1/2} S_{ij}^v(\vartheta), \tag{7}$$

where $K_v$ ($v = 1, 2$) are the stress-intensity factors related to mode 1 (opening) and mode 2 (sliding) respectively. Analogously to eqn (2), they can be expressed as

$$K_v = \sigma b^{1/2} f_v(a/b); \quad v = 1, 2. \tag{8}$$

The interaction of the two fundamental fracture modes produces crack propagation when a function of $K_v$ ($v = 1, 2$) is equal to its critical value (Carpinteri, Di Tommaso and Viola, 1979):

$$F(K_v; v = 1, 2) = \text{constant}. \tag{9}$$

Most relevant fracture criteria can be approximated by an elliptic function $F$ (Di Leonardo, 1979):

$$K_1^2 + q K_2^2 = K_c^2, \tag{10}$$

where $q \geqslant 0$ is a measure of the influence of mode 2 on crack propagation. Substituting eqn (8) into eqn (10), it follows that

$$\sigma^2 b[f_1^2 + q f_2^2] = K_c^2, \tag{11}$$

and, therefore, the failure stress may be expressed by eqn (3) again, with function $f$ replaced by the square root:

$$f = \sqrt{f_1^2 + q f_2^2}. \tag{12}$$

Thus, even in the case of a mixed mode Griffith crack, the scale effect is represented by a straight line with slope $-1/2$ in the plane $\ln \sigma_f - \ln b$ (Fig. 2(a)). This means that it is the power of the stress-singularity—and not the geometry of crack, structure and load—which defines the rate of strength decrease by increasing the size-scale.

Let us consider now a two-dimensional linear-elastic structure with a re-entrant corner of amplitude $\gamma$ (Fig. 1(c)). Williams (1952) proved that when both the notch surfaces are free, the symmetrical stress field at the notch tip is
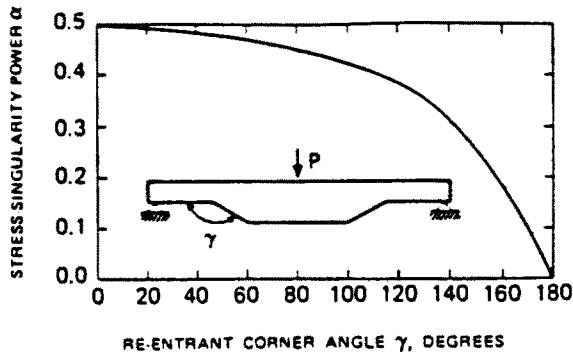
Fig. 3. Stress-singularity power vs re-entrant corner angle.

$$\sigma_{ij} = K^* r^{-\alpha} S_{ij}^{(\gamma)} (\vartheta),$$ (13)

where the power $\alpha$ of the stress-singularity ranges between $1/2$ (when $\gamma = 0$) and 0 (when $\gamma = \pi$), as shown in Fig. 3. If Buckingham's Theorem for physical similarity and scale modelling is applied, and stress and linear size are assumed as fundamental quantities (Carpinteri, 1982a), it will be possible to write an equation analogous to eqn (2):

$$K^* = \sigma b^{\alpha} g(a/b).$$ (14)

When angle $\gamma$ vanishes, eqn (14) coincides with eqn (2), whereas when $\gamma = \pi$, the stress-singularity disappears and the stress-intensity factor $K^*$ assumes the physical dimensions of a stress and becomes proportional to the nominal stress $\sigma$. As experimentally demonstrated by Leicester (1973), the failure stress $\sigma_f$ is achieved when the $K^*$-factor is equal to its critical value $K_c^*$:

$$\sigma_f = K_c^* b^{-\alpha} \frac{1}{g(a/b)},$$ (15)

or, in logarithmic form,

$$\ln \sigma_f = B(K_c^*, a/b) - \alpha \ln b,$$ (16)

where

$$B(K_c^*, a/b) = \ln K_c^* - \ln g(a/b).$$ (17)

If we keep material and structural shape constant and take into consideration a set of similar structures (Fig. 1(c)), the strength $\ln \sigma_f$ turns out to be a linearly decreasing function with slope $-\alpha$ of the scale-parameter $\ln b$ (Fig. 2(b)). When $\gamma \to \pi$, i.e. when $\alpha \to 0$, any scale effect vanishes and the straight line becomes horizontal. In this case the equilibrium condition is:

$$\sigma b = K^* (b-a),$$ (18)

and then, from eqn (14),

$$g(a,b) = \frac{1}{1 - \frac{a}{b}}. \tag{19}$$

When the notch depth $a/b$ tends to zero, the shape-function $g(a/b) = 1$ and the stress-intensity factor $K^*$ coincides with the nominal stress $\sigma$ exactly—see eqn (14). The distinction between ultimate strength collapse and fracture at the corner vanishes and condition (16) coincides with condition (6).

The case of a re-entrant corner subjected to mixed mode loading can be handled in the same way as the Griffith crack. Even in this case, the conclusion is that only the power of the stress-singularity, and not the loading condition, determines the rate of decrease in strength with size.

Let us now consider a two-dimensional linear-elastic structure with a polygonal void of regular shape and arbitrary number of sides $M$ (Fig. 1(d)). As is well known, the angle $\gamma$ is a function of the number of sides $M$:

$$\gamma = \pi\left(\frac{M-2}{M}\right). \tag{20}$$

Every re-entrant corner of the polygonal void is generally subjected to a mixed mode loading condition with a stress-singularity $r^{-\lambda}$. For a given external load, there is a corner tip which is subjected to the most severe stress field. If the load is increased proportionally, the fracture condition will first be achieved at this tip. On the basis of what has been said previously about mixed mode cracks and notches, the strength varies according to eqn (16) even in this case, and the intercept is

$$B\left(K_c^*, \frac{a}{b}\right) = \ln K_c^* - \ln \sqrt{g_1^2 + q g_2^2}, \tag{21}$$

with obvious meanings of the symbols. A graph of $\ln \sigma_f$ versus $\ln b$ is therefore linear with slope $-\alpha$, even in the case of polygonal void. For $M = 2$ we have a Griffith crack, eqn (20) giving $\gamma = 0$, whereas for $M \to \infty$ the polygonal void becomes a circular hole, eqn (20) giving $\gamma = \pi$. In the latter case, any size effect vanishes and the $\ln \sigma_f - \ln b$ graph appears horizontal. On the other hand, it is well known that the stress-concentration factor is independent of the size of the circular hole and that its value is 3.

### 3. INFLUENCE OF DEFECTS AND POROSITY ON MICROCRACKING INITIATION AND TENSILE STRENGTH

In the present section, two-dimensional structures with a multitude of cracks or voids of a given size-distribution are considered. Three hypotheses are assumed:

(1) the structure is macroscopically homogeneous;
(2) the structure is macroscopically isotropic;
(3) the interaction among the imperfections is negligible.

As a first case, let us consider a set of similar structures, where a multitude of cracks and/or polygonal voids of constant size $a$ are embedded (Fig. 4(a)). They can be considered as specimens of the same material, and their failure occurs when the fracture condition at the imperfection of the most critical orientation is realized. Since such imperfections are all the same size, we can assert that any size effect is absent in this ideal case.

Let us consider now a set of similar structures, where the imperfections have a constant size which is proportional to the size of the structure (Fig. 4(b)). In this case, they cannot be considered as specimens of the same material. The failure occurs at the imperfection of the most critical orientation, which is of a size proportional to the size of the structure. Since the influence of the other imperfections is assumed negligible, this case is completely
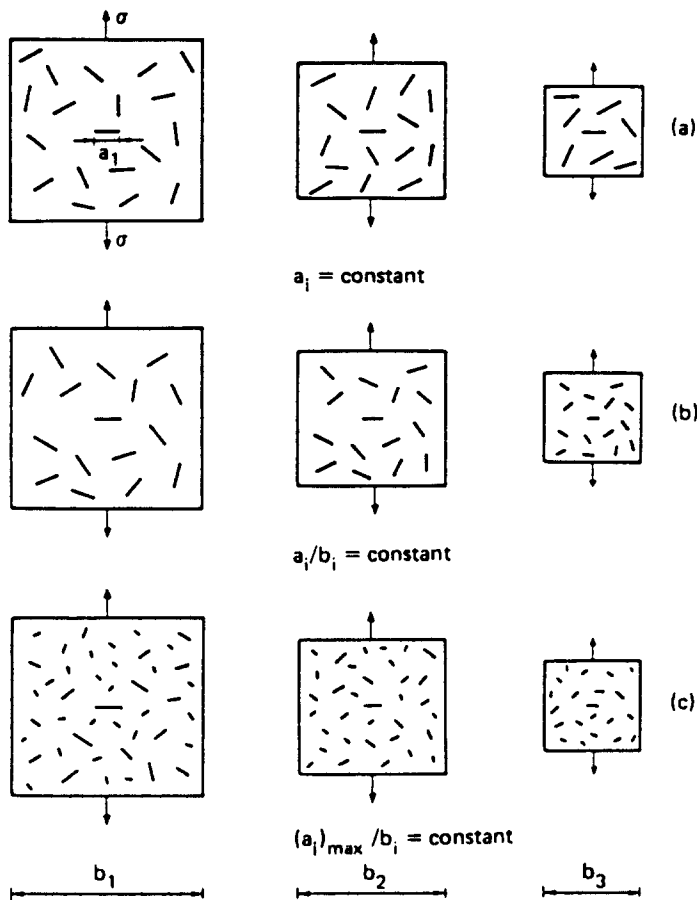
Fig. 4. Geometrically similar structures with many random defects: (a) constant defect size; (b) defect size constant and proportional to the structural size; (c) defect size distribution of proportionality.

equivalent to that of a unique imperfection of size proportional to that of the structure. Thus, the strength size effect is represented by a linear $\ln \sigma_f$–$\ln b$ diagram with slope $-\alpha$, where $\alpha$ is the power of the stress-singularity produced by the imperfections. If we have imperfections of the same size, but with different shape (e.g. cracks and circular pores), the fracture condition has to be evaluated only for the imperfections with the maximum value of $\alpha$ ($0 \leqslant \alpha \leqslant 1/2$).

Let us consider finally a set of similar structures where the imperfections with the most dangerous shape ($\alpha = \alpha_{max}$) have a probability density $p(a)$ of size distribution (Figs. 4(c) and 5(a)). We can assert that if the size distribution $p(a)$ is such that the maximum size $a_{max}$ is proportional to the linear scale $b$, then the strength size effect will be represented by a linear $\ln \sigma_f$–$\ln b$ diagram with slope $-\alpha_{max}$. The above hypothesis is very restrictive and is valid only when the probability density of size distribution $p(a)$ presents particular properties. If $\rho$ is the density of imperfections (number of imperfections per unit area), the maximum size $a_{max}$ can be defined as follows:

$$\rho b^2 p(a_{max}) \frac{1}{2\pi} \Delta a \Delta \omega = 1, \tag{22}$$

where the factor $(1/2\pi)$ is due to the fact that all the imperfection orientation angles $\omega$ are equally likely. If a geometrically similar structure of characteristic size $kb$ is considered and the above hypothesis is assumed (Fig. 4(c)), we can write
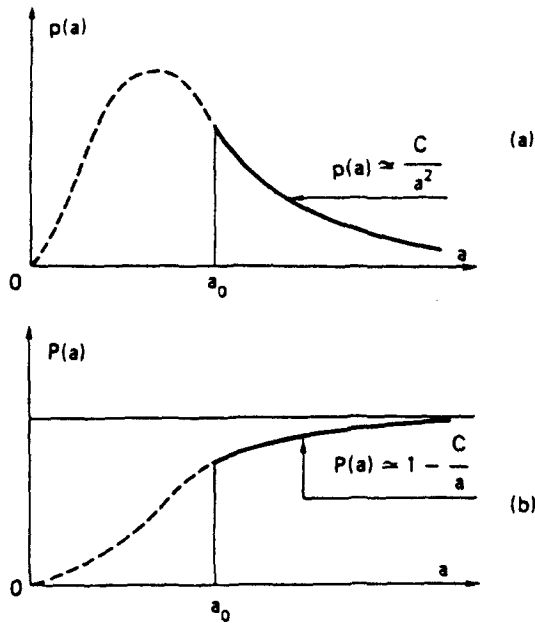
Fig. 5. Defect size distribution of proportionality: (a) probability density; (b) cumulative distribution.

$$\rho(kb)^2 p(ka_{max}) \frac{1}{2\pi} \Delta a\, \Delta\omega = 1. \tag{23}$$

Since $a_{max}$ is a function of $\rho$ and $b$, besides the ranges $\Delta a$ and $\Delta\omega$, it follows that eqns (22) and (23) must be valid for any defect size $a$:

$$\rho b^2 p(a) \frac{1}{2\pi} \Delta a\, \Delta\omega = 1, \tag{24}$$

$$\rho k^2 b^2 p(ka) \frac{1}{2\pi} \Delta a\, \Delta\omega = 1. \tag{25}$$

From eqns (24) and (25) it follows that

$$p(a) = k^2 p(ka), \quad \forall a \gg \bar{a}, \quad \forall k \in R^+, \tag{26}$$

and then function $p$ assumes the form

$$p(a) = \frac{C}{a^2}, \quad \forall a \gg \bar{a}, \tag{27}$$

where $C$ is a constant with the physical dimension of a length and $\bar{a}$ is the average defect size. Equation (27) will be referred to as the defect size distribution of proportionality. The related cumulative distribution function $P$ is

$$P(a) = \int_0^a p(x)\, dx = \int_0^{a_0} p(x)\, dx + \int_{a_0}^a \frac{C}{x^2}\, dx, \tag{28}$$

where $a_0 \gg \bar{a}$ is the value beyond which the decreasing branch of function $p$ can be approximated by eqn (27). Carrying out the integrations in eqn (28), we obtain

$$P(a) = P_0 + \left[ -\frac{C}{x} \right]_{a_0}^{a} = P_0 + \frac{C}{a_0} - \frac{C}{a}. \tag{29}$$

Since for $a \to \infty$ the cumulative distribution $P(a) \to 1$,

$$P_0 + \frac{C}{a_0} = 1, \tag{30}$$

and then (Fig. 5(b)):

$$P(a) = 1 - (C/a), \quad \text{for} \quad a > a_0. \tag{31}$$

with

$$C = (1 - P_0)a_0. \tag{32}$$

Generally speaking, the cumulative distribution function $P$ will have the following form:

$$P(a) = 1 - \frac{C}{a^N}, \quad \text{for } a > a_0, \tag{33}$$

with

$$C = (1 - P_0)a_0^N. \tag{34}$$

In this case, the strength size effect can be represented by a linear $\ln \sigma_f$–$\ln b$ diagram with slope $-\alpha_N$:

$$\alpha_N(\gamma, N) = \frac{\alpha(\gamma)}{N^\zeta}, \tag{35}$$

where the exponent $\zeta$ depends on the secondary features of the material (e.g. density of imperfections, size distributions of the less dangerous defects, etc.). The probability density of size distribution in the general case—see eqn (33)—is:

$$p(a) = \frac{dP}{da} = N \frac{C}{a^{N+1}}, \quad \text{for} \quad a > a_0, \tag{36}$$

which becomes eqn (27) when $N = 1$.

Equation (35) shows that the size effect vanishes when $\gamma = \pi$ (circular pores) and/or when $N \to \infty$ (nearly constant defect size). On the other hand, the size effect becomes enormous when $N \to 0$ (very large dispersion in the imperfection size distribution). The treatment of 2-D structures can formally be extended to 3-D structures with polyhedral voids (Carpinteri, 1983).

If the preceding assumptions are valid, the experimental $\ln \sigma_f$–$\ln b$ strength diagram must appear linear with a negative slope $\alpha_N$, according to eqn (35). When the dispersion in the imperfection size distribution is not very high ($N \geqslant 1$), we have the theoretical upper bound $\alpha_N \leqslant 0.50$, which is rarely exceeded in the experimental results reported in the relevant literature.
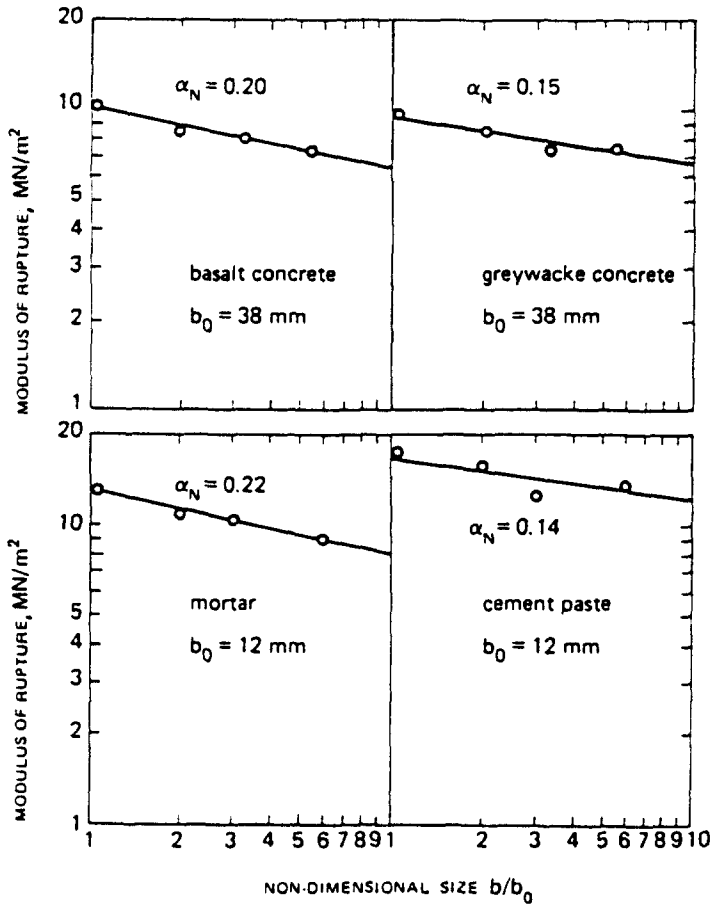
Fig. 6. Effect of size on flexural tensile strength of cementitious materials.

The results of Strange and Bryant (1979) are plotted in Fig. 6. The graph of flexural tensile strength against the beam width shows a very regular linear decrease in the bilogarithmic diagram for all the four cement composites investigated. The results of Sabnis and Mirza (1979) show the same trend for the flexural tensile strength (Fig. 7) and for the indirect tensile strength (Fig. 8).
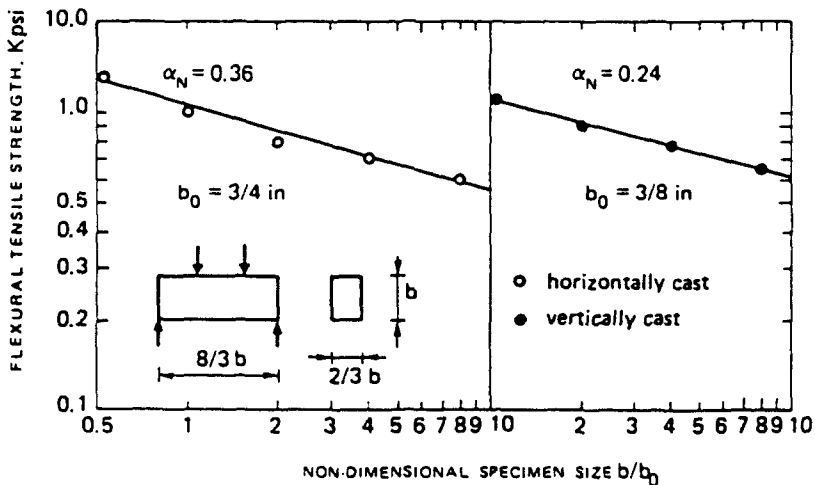


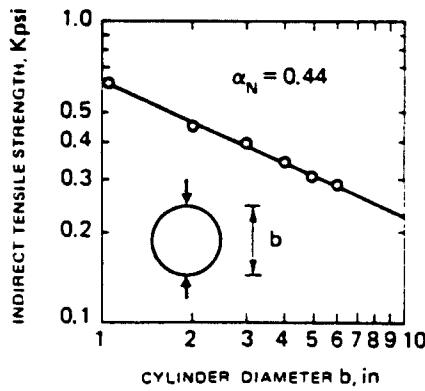Fig. 7. Effect of size on flexural tensile strength of concrete.

Fig. 8. Effect of size on indirect tensile strength of concrete.

## 4. UNIAXIAL TENSILE LOADING OF SLABS AND STRAIN LOCALIZATION

Let us consider an elastic-softening material with a double constitutive law : (a) tension $\sigma$ vs dilatation $\varepsilon$; (b) tension $\sigma$ vs crack opening displacement $w$, after reaching the ultimate tensile strength $\sigma_u$ or strain $\varepsilon_u = \sigma_u/E$ (Fig. 9) :

$$\sigma = E\varepsilon, \qquad \text{for } \varepsilon \leqslant \varepsilon_u, \tag{37a}$$

$$\sigma = \sigma_u\left(1 - \frac{w}{w_c}\right), \quad \text{for } w \leqslant w_c, \tag{37b}$$

$$\sigma = 0, \qquad \text{for } w > w_c. \tag{37c}$$

According to eqn (37c), the cohesive interaction between the crack surfaces vanishes for distances larger than the critical opening $w_c$.

If a plane slab is increasingly loaded, the deformation history will undergo three different stages.

(1) The slab behaves elastically without damage or fracture zones (Fig. 10(a)). The displacement of the upper edge is

$$\delta = \frac{\sigma}{E}l, \quad \text{for } \varepsilon \leqslant \varepsilon_u. \tag{38}$$

(2) After reaching the ultimate tensile strength $\sigma_u$, a fracture cohesive zone develops in the weakest section of the slab. Observe that, as the stress field is homogeneous, another
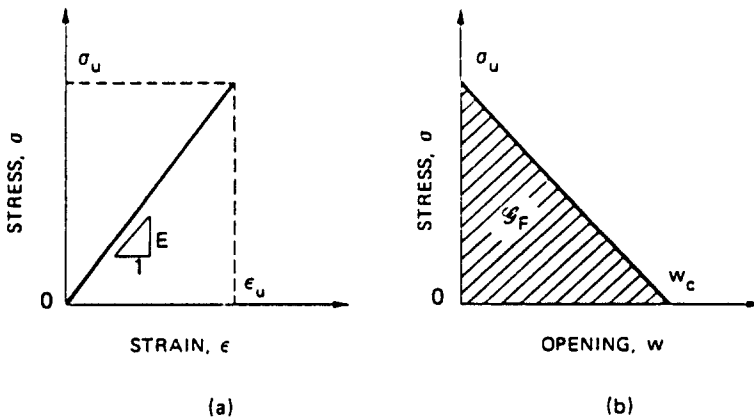


(a)                    (b)

Fig. 9. (a) Stress-strain elastic law; (b) stress vs crack opening displacement cohesive law.
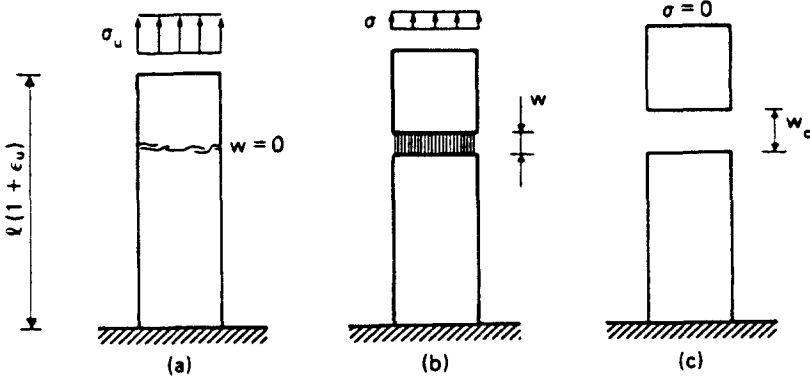
Fig. 10. Three different stages of the deformation history: (a) no damage; (b) strain localization; (c) separation.

cause of inhomogeneity must be assumed for strain-localization. The slab behaves elastically only outside the fracture zone (Fig. 10(b)). The displacement of the upper edge is

$$\delta = \frac{\sigma}{E}l + w, \quad \text{for} \quad w \leqslant w_c. \tag{39}$$

Recalling eqn (37b), eqn (39) gives:

$$\delta = \frac{\sigma}{E}l + w_c\left(1 - \frac{\sigma}{\sigma_u}\right), \quad \text{for} \quad w \leqslant w_c. \tag{40}$$

While the fracture zone opens, the elastic zone shrinks at progressively decreasing stresses. At this stage, the loading process may be stable only if it is displacement-controlled, i.e. if the external displacement $\delta$ is imposed. But this is only a necessary and not a sufficient condition for stability.

(3) When $\delta > w_c$, the reacting stress $\sigma$ vanishes, the cohesive forces disappear and the slab is completely separated into two pieces (Fig. 10(c)).

Rearranging eqn (38) gives:

$$\sigma = E\frac{\delta}{l}, \quad \text{for} \quad \delta \leqslant \varepsilon_u l. \tag{41}$$

while the condition of complete separation (stage 3) becomes:

$$\sigma = 0, \quad \text{for} \quad \delta \geqslant w_c. \tag{42}$$

When $w_c > \varepsilon_u l$, the softening process is stable only if displacement-controlled, since
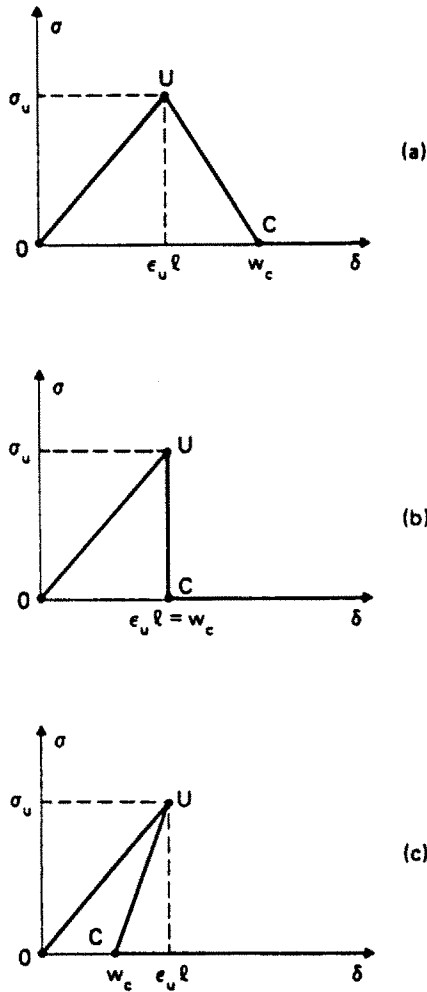
Fig. 11. Stress–displacement response: (a) normal softening; (b) and (c) catastrophic softening (snap back).

the slope $d\sigma/d\delta$ at stage (2) is negative (Fig. 11(a)). When $w_c = \varepsilon_u l$, the slope $d\sigma/d\delta$ is infinite, and a drop in the loading capacity occurs, even if the loading is displacement-controlled (Fig. 11(b)). Eventually, when $w_c < \varepsilon_u l$, the slope $d\sigma/d\delta$ becomes positive (Fig. 11(c)) and the same negative jump occurs, like that shown in Fig. 11(b).

Rearranging eqn (40) gives:

$$\delta = w_c + \sigma\left(\frac{l}{E} - \frac{w_c}{\sigma_u}\right). \tag{43}$$

The conditions just obtained from a geometrical point of view (Fig. 11) may be obtained also from the analytical derivation of eqn (43).

Normal softening occurs for $d\delta/d\sigma < 0$:

$$\left(\frac{l}{E} - \frac{w_c}{\sigma_u}\right) < 0, \tag{44}$$

whereas catastrophic softening (or snap-back) occurs for $d\delta/d\sigma \geqslant 0$:

$$\left(\frac{l}{E} - \frac{w_c}{\sigma_u}\right) \geqslant 0. \tag{45}$$

Equation (45) may be rearranged in the following form:

$$\frac{(w_c/2b)}{\varepsilon_u(l/b)} \leqslant \frac{1}{2}, \tag{46}$$

where $b$ is the slab width.

The ratio $(w_c/2b)$ is a dimensionless number, which is a function of material properties and structural size scale (Carpinteri, 1985):

$$s_E = \frac{w_c}{2b} = \frac{\mathcal{G}_F}{\sigma_u b}. \tag{47}$$

$\mathcal{G}_F = \frac{1}{2}\sigma_u w_c$ being the fracture energy of the material (Fig. 9). The energy brittleness number $s_E$ describes the scale effects of fracture mechanics, i.e. the ductile–brittle transition when the size-scale is increased. Equation (46) may be presented in the following final form:

$$\frac{s_E}{\varepsilon_u \lambda} \leqslant \frac{1}{2}, \tag{48}$$

with $\lambda$, the slenderness, equal to $l/b$.

When the size-scale and slab slenderness are relatively large and the fracture energy relatively low, the gobal structural behaviour is brittle. Not the independent values of parameters $s_E$, $\varepsilon_u$ and $\lambda$, but only their combination $B = s_E/\varepsilon_u \lambda$ is responsible for the global brittleness or ductility of the structure considered.

When $B \leqslant 1/2$, the plane rectangular slab of Fig. 10 shows a mechanical behaviour which can be defined as *brittle* or *catastrophic*. A *bifurcation* or *snap-back* of the global equilibrium occurs since, if point U in Fig. 11(c) is reached and then the imposed external displacement $\delta$ is decreased by a very small amount $d\delta$, the global unloading may occur along two alternative paths—the elastic path UO or the virtual softening path UC.

## 5. THREE POINT BENDING OF BEAMS AND CURVATURE LOCALIZATION

The linear-elastic behaviour of a three point bending initially uncracked beam may be represented by the following dimensionless equation:

$$\tilde{P} = \frac{4}{\lambda^3} \tilde{\delta} \tag{49}$$

where the dimensionless load and central deflection are respectively given by:

$$\tilde{P} = \frac{Pl}{\sigma_u t b^2}, \tag{50}$$

$$\tilde{\delta} = \frac{\delta l}{\varepsilon_u b^2}, \tag{51}$$

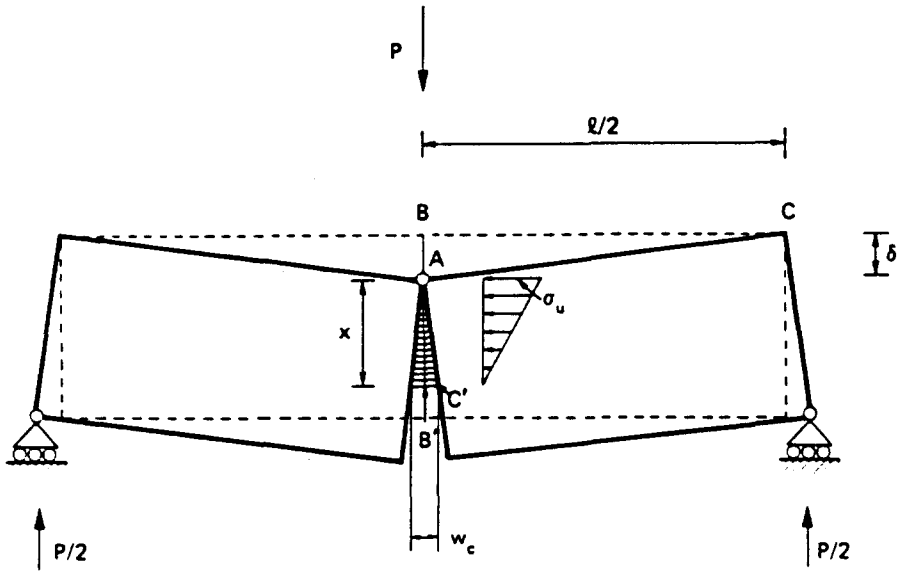with $l$ = beam span, $b$ = beam depth and $t$ = beam thickness.

Fig. 12. Limit-situation of concrete fracture with cohesive forces.

Once the ultimate tensile strength $\sigma_u$ is achieved at the lower beam edge, a fracturing process in the central cross-section is presumed to start. Such a process admits a limit-situation like that in Fig. 12. The limit stage of the fracturing and deformation process may be considered as that of two rigid parts connected by the hinge $A$ in the upper beam edge. The equilibrium of each part is ensured by the external load, the support reaction and the closing cohesive forces. The latter depend on the distance between the two interacting surfaces: with increasing distance $w$, the cohesive forces decrease until they vanish for $w \geqslant w_c$.

The geometrical similarity of the triangles $ABC$ and $AB'C'$ in Fig. 12 makes

$$\frac{\delta}{l/2} = \frac{w_c/2}{x},\tag{52}$$

where $x$ is the extension of the triangular distribution of cohesive forces. Equation (52) can be rearranged as:

$$x = \frac{w_c l}{4\delta}.\tag{53}$$

Rotational equilibrium about point A is possible for each beam part only if their respective moments of support reaction and cohesive forces are equal:

$$\frac{P}{2}\frac{l}{2} = \frac{\sigma_u x t}{2}\frac{x}{3}.\tag{54}$$

Recalling eqn (53), the relation between load and deflection may be obtained:

$$P = \frac{\sigma_u t l w_c^2}{24}\frac{1}{\delta^2}.\tag{55}$$

Equation (55) can be put into dimensionless form:

$$\tilde{P} = \frac{1}{6}\left(\frac{s_E \lambda^2}{\varepsilon_u \delta}\right)^2.$$ (56)

While the linear equation (49) describes the elastic behaviour of the beam when initially uncracked, the hyperbolic equation (56) represents the asymptotic behaviour of the same beam when totally cracked. Equation (49) is valid only for load values lower than that producing the ultimate tensile strength $\sigma_u$ at the lower beam edge:

$$\tilde{P} \leqslant \frac{2}{3}.$$ (57)

On the other hand, eqn (56) is valid only for deflection values higher than that producing a cohesive zone of extension $x$ equal to the beam depth $b$:

$$x \leqslant b.$$ (58)

From eqns (53) and (58), it follows that

$$\tilde{\delta} \geqslant \frac{s_E \lambda^2}{2\varepsilon_u}.$$ (59)

The bounds (57) and (59), upper for load and lower for deflection respectively, can be transformed into two equivalent bounds, upper for both deflection and load. Equations (49) and (57) imply that

$$\tilde{\delta} \leqslant \frac{\lambda^3}{6}.$$ (60)

whereas eqns (56) and (59) imply that

$$\tilde{P} \leqslant \frac{2}{3}.$$ (61)

Conditions (57) and (61) are coincident. Therefore, a stability criterion for elastic-softening beams may be obtained by comparing eqns (59) and (60). When the two domains are separated, it is reasonable to presume that the two $P$-$\delta$ branches—linear and hyperbolic—are connected by a regular curve (Fig. 13(a)). On the other hand, when the two
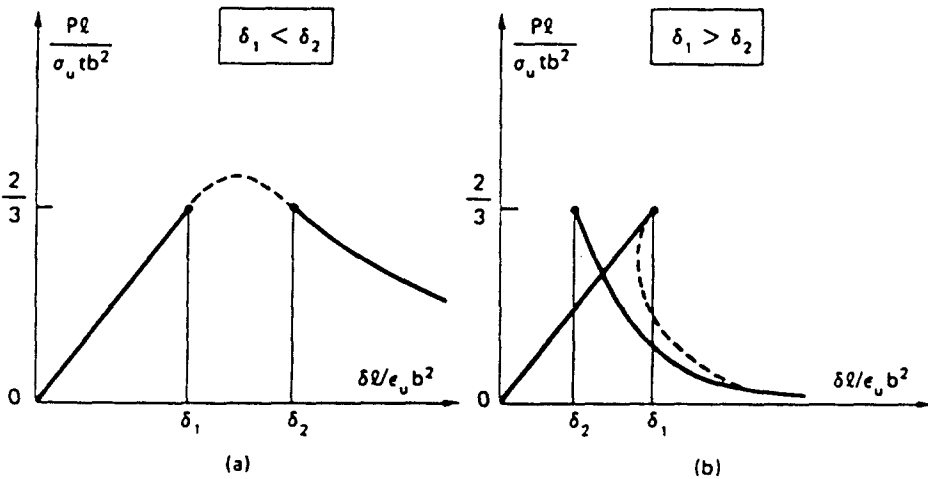


Fig. 13. Load-deflection diagrams: (a) ductile condition; (b) brittle condition. $\delta_1 = \lambda^3/6$; $\delta_2 = s_E \lambda^2/2\varepsilon_u$.
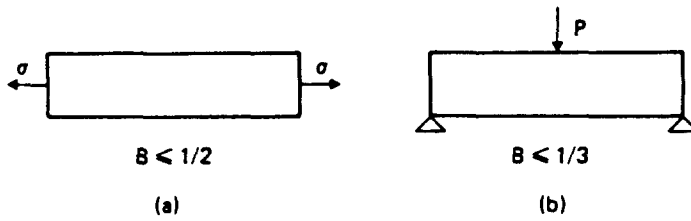
Fig. 14. Bounds to relative brittleness for (a) uniaxial tension and (b) three point bending geometry.
$B = s_E/\varepsilon_u \lambda.$

domains are partially overlapping, it is well-founded to suppose them to be connected by a curve with highly negative or even positive slope (Fig. 13(b)).

Unstable behaviour and catastrophic events (snap-back) are then expected for

$$\frac{s_E \lambda^2}{2\varepsilon_u} \leqslant \frac{\lambda^3}{6}. \tag{62}$$

and the brittleness condition for the three point bending geometry becomes:

$$\frac{s_E}{\varepsilon_u \lambda} \leqslant \frac{1}{3}. \tag{63}$$

Even in this case, the system is brittle for low brittleness numbers $s_E$, high ultimate strains $\varepsilon_u$ and large slendernesses $\lambda$. Observe that the same dimensionless number $B = s_E/\varepsilon_u \lambda$ appears also in eqn (48), where the upper bound for brittleness is equal to 1/2.

It is therefore evident that the relative brittleness for a structure is dependent on loading condition and external constraints, in addition to the material properties, size-scale and slenderness. For instance, uniaxial tension is more unstable than three point bending (Fig. 14).

## 6. APPARENT DECREASE IN THE ULTIMATE BENDING STRENGTH OF INITIALLY UNCRACKED MATERIALS

The cohesive crack model is based on the following assumptions (Hillerborg *et al.*, 1976; Carpinteri, 1985; Carpinteri and Fanelli, 1987):

(1) The cohesive fracture zone (plastic or process zone) begins to develop when the maximum principal stress achieves the ultimate tensile strength $\sigma_u$ (Fig. 9(a)).

(2) The material in the process zone is partially damaged but still able to transfer stress. Such a stress is dependent on the crack opening displacement $w$ (Fig. 9(b)).

The real crack tip is defined as the point where the distance between the crack surfaces is equal to the critical value of crack opening displacement $w_c$ and where the normal stress vanishes (Fig. 15(a)). On the other hand, the fictitious crack tip is defined as the point where the normal stress attains the maximum value $\sigma_u$ and the crack opening vanishes (Fig. 15(a)).

The closing stresses acting on the crack surfaces (Fig. 15(a)) can be replaced by nodal forces (Fig. 15(b)). The intensity of these forces depends on the opening of the fictitious crack, $w$, according to the $\sigma$–$w$ constitutive law of the material (Fig. 9(b)). When the tensile strength $\sigma_u$ is achieved at the fictitious crack tip (Fig. 15(b)), the top node is opened and a cohesive force starts acting across the crack, while the fictitious crack tip moves to the next node.

With reference to the three point bending test (TPBT) geometry in Fig. 16, the nodes are distributed along the potential fracture line. The coefficients of influence in terms of node openings and deflection are computed by a finite element analysis where the fictitious
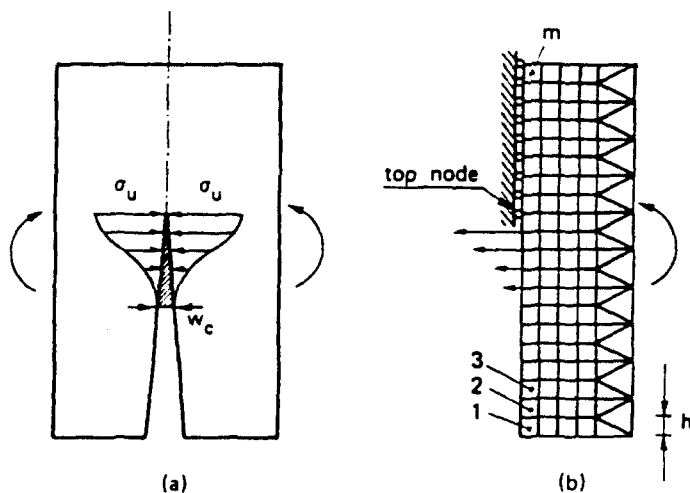
Fig. 15. Stress distribution across the cohesive zone (a) and equivalent nodal forces in the finite
element mesh (b).

structure in Fig. 16 is subjected to $(n + 1)$ different loading conditions. Consider the TPBT
in Fig. 17(a) with the initial crack of length $a_0$ whose tip is at node $k$. The crack opening
displacements at the $n$ fracture nodes may be expressed as follows:

$$w = KF + CP + \Gamma,  \tag{64}$$

where $w$ is the vector of the crack opening displacements, $K$ the matrix of the coefficients
of influence (nodal forces), $F$ the vector of the nodal forces, $C$ the vector of the coefficients
of influence (external load), $P$ the external load and $\Gamma$ is the vector of the crack opening
displacements due to the specimen weight.

On the other hand, the initial crack is stress-free, and therefore

$$F_i = 0, \quad \text{for} \quad i = 1, 2, \ldots, (k-1),  \tag{65a}$$

while at the ligament there is no displacement discontinuity:

$$w_i = 0, \quad \text{for} \quad i = k, (k+1), \ldots, n.  \tag{65b}$$

Equations (64) and (65) constitute a linear algebraic system of $2n$ equations in $2n$
unknowns—the elements of vectors $w$ and $F$. If load $P$ and vector $F$ are known, it is possible
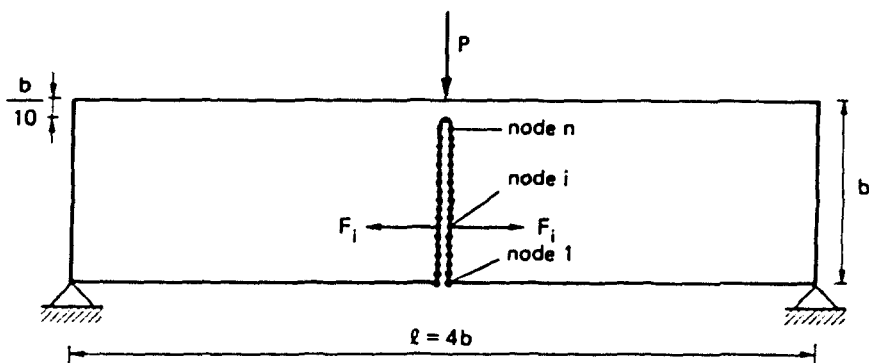to compute the beam deflection, $\delta$:



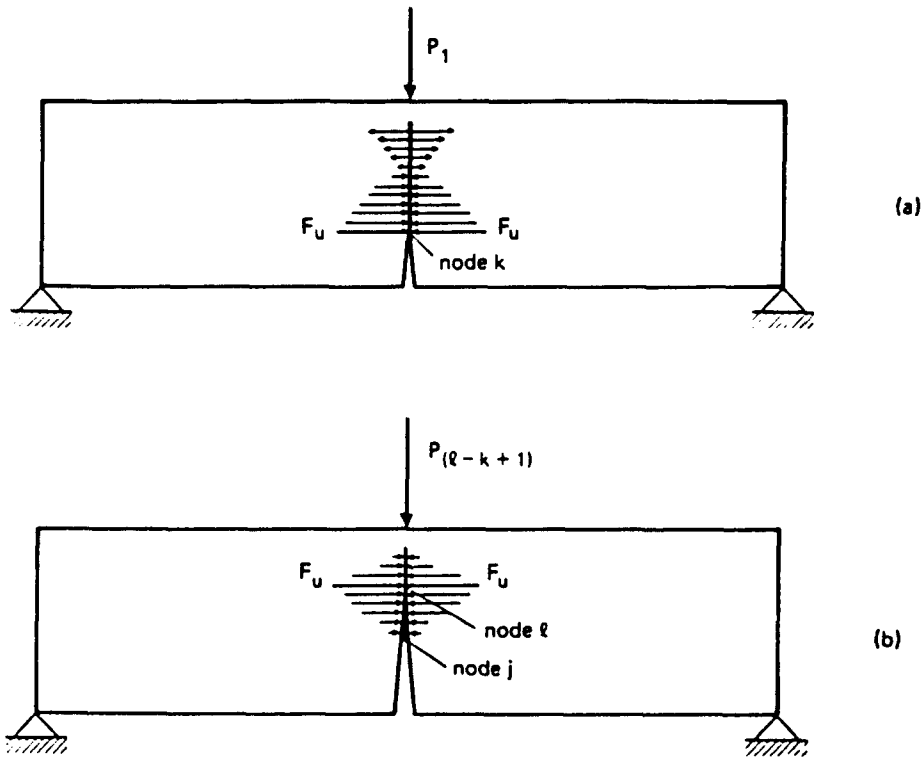Fig. 16. Finite element nodes along the potential fracture line.

Fig. 17. Cohesive crack configurations at the first (a) and $(l-k+1)$th (b) crack growth increment.

$$\delta = \mathbf{C}^r \mathbf{F} + D_P P + D_\gamma,\tag{66}$$

where $D_P$ is the deflection for $P = 1$ and $D_\gamma$ is the deflection due to the specimen weight.

After the first step, a cohesive zone forms in front of the real crack tip (Fig. 17(b)), say between nodes $j$ and $l$. Then eqns (65) are replaced by

$$F_i = 0, \qquad\qquad \text{for } i = 1, 2, \ldots, (j-1),\tag{67a}$$

$$F_i = F_u\left(1 - \frac{w_i}{w_c}\right), \quad \text{for } i = j, (j+1), \ldots, l,\tag{67b}$$

$$w_i = 0, \qquad\qquad \text{for } i = l, (l+1), \ldots, n,\tag{67c}$$

where $F_u$ is the ultimate strength nodal force (Fig. 15(b)):

$$F_u = b\sigma_u/m.\tag{68}$$

Equations (64) and (67) constitute a linear algebraic system of $(2n+1)$ equations and $(2n+1)$ unknowns—the elements of vectors $\mathbf{w}$ and $\mathbf{F}$ and the external load $P$. At the first step, the cohesive zone is missing $(l = j = k)$ and the load $P_1$ producing the ultimate strength nodal force $F_u$ at the initial crack tip (node $k$) is computed. Such a value $P_1$, together with the related deflection $\delta_1$ computed through eqn (66), gives the first point of the $P$-$\delta$ curve. At the second step, the cohesive zone is between the nodes $k$ and $(k+1)$, and the load $P_2$ producing the force $F_u$ at the second fictitious crack tip (node $k+1$) is computed. Equation (66) then provides the deflection $\delta_2$. At the third step, the fictitious crack tip is at the node $(k+2)$, and so on. The present numerical program simulates a loading process where the controlling parameter is the fictitious crack depth. On the other hand, real (or stress-free) crack depth, external load and deflection are obtained at each step after an iterative procedure.
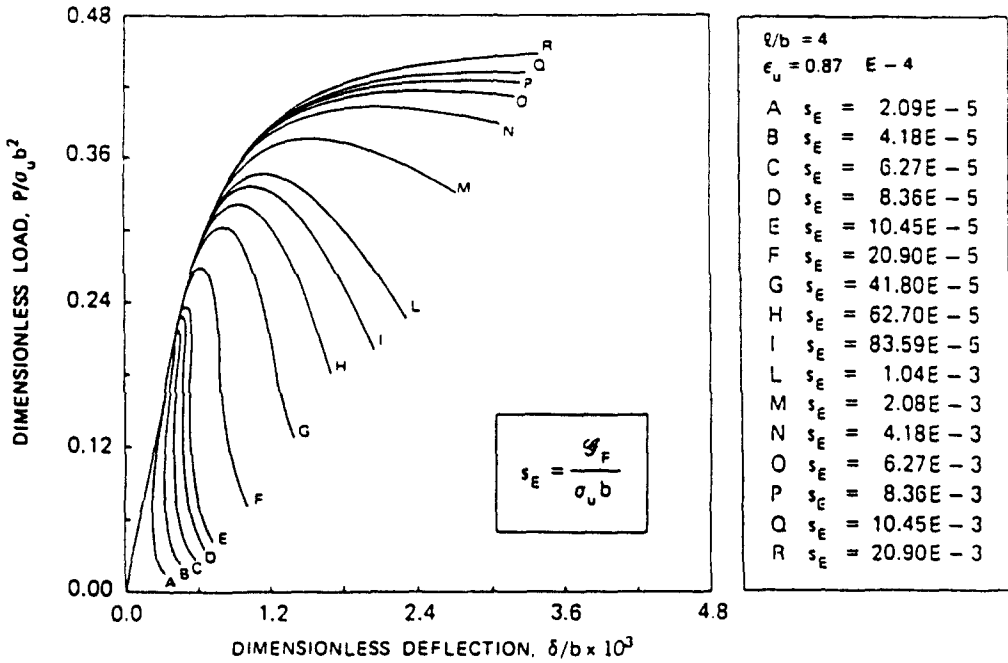
Fig. 18. Dimensionless load-deflection diagrams with various brittleness numbers $s_E = \mathscr{G}_F / \sigma_u b$ ($\lambda = 4$, $a_0/b = 0.0$, $\varepsilon_u = 0.87 \times 10^{-4}$).

The program stops with the untying of the node $n$ and, consequently, with the determination of the last couple of values $F_n$ and $\delta_n$. In this way, the complete load-deflection curve is automatically plotted by the computer.

Some dimensionless load-deflection diagrams for a concrete-like material are plotted in Fig. 18, with $a_0/b = 0.0$, $\varepsilon_u = 0.87 \times 10^{-4}$, $\nu = 0.1$, $t = b$ and $l = 4b$, and with various values of the non-dimensional number $s_E$. The specimen behaviour is brittle (snap-back) for low $s_E$ numbers—i.e. for low fracture toughnesses $\mathscr{G}_F$, high tensile strengths $\sigma_u$ and/or large sizes $b$. For $s_E \leqslant 10.45 \times 10^{-5}$, the $P$–$\delta$ curve has a positive slope in the softening branch, and a catastrophic event occurs if the loading process is deflection-controlled. Such an indenting branch is not virtual only if the loading process is controlled by a monotonically increasing function of time—for example, the displacement discontinuity across the crack (Fairhurst et al., 1971; Rokugo et al., 1986; Biolzi et al., in press). On the other hand, eqn (63) gives $s_E \leqslant 11.60 \times 10^{-5}$. Such a condition reproduces that shown in Fig. 18 very accurately. When the post-peak behaviour is kept under control up to complete structure separation, the area delimited by the load–deflection curve and the deflection axis represents the product of the fracture toughness $\mathscr{G}_F$ and the initial cross-sectional area $bt$.

The maximum loading capacity $P_{max}^{(1)}$ of initially uncracked specimens with $l = 4b$ is obtained from Fig. 18. On the other hand, the maximum load $P_{max}^{(3)}$ of the ultimate strength is given by:

$$P_{max}^{(3)} = \frac{2}{3} \frac{\sigma_u t b^2}{l}.$$                    (69)

The values of the ratio $P_{max}^{(1)}/P_{max}^{(3)}$ may also be regarded as the ratio of the apparent tensile strength $\sigma_f$ (given by the maximum load $P_{max}^{(1)}$ and by applying eqn (69)) to the true tensile strength $\sigma_u$ (considered as a material constant). It is evident from Fig. 19 that the results of the cohesive crack model tend to those of the ultimate strength analysis for low $s_E$ values:

$$\lim_{s_E \to 0} P_{max}^{(1)} = P_{max}^{(3)}.$$                    (70)

Therefore, for comparatively large specimen sizes only, the tensile strength $\sigma_u$ can be
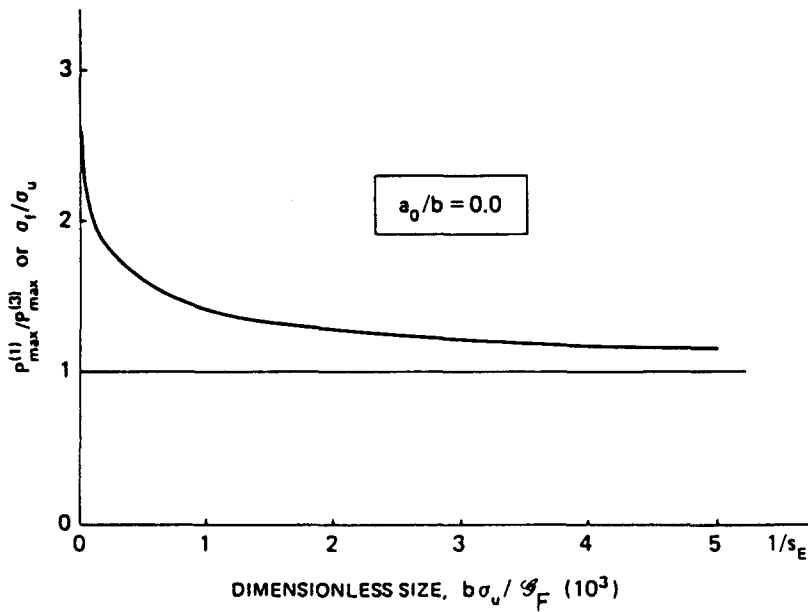
Fig. 19. Decrease in apparent strength by increasing the specimen size ($\lambda = 4$, $a_0/b = 0.0$, $\varepsilon_u = 0.87 \times 10^{-4}$).

obtained as $\sigma_u = \sigma_f$. With the usual laboratory specimens, an apparent strength higher than the true one is always found (Petersson, 1981).

As a limiting case, for the size $b \to 0$ or fracture energy $\mathcal{G}_F \to \infty$ (elastic–perfectly plastic material in tension), i.e. for $s_E \to \infty$, the apparent strength $\sigma_f \to 3\sigma_u$. In fact, in the center of the beam, the uniform stress distribution (Fig. 20) produces a plastic hinge with a resistant moment $M_{max}$ which is twice the classical moment of the bi-rectangular limit stress distribution (elastic–perfectly plastic material in tension and compression).

The diagrams in Fig. 21 are related to a higher beam slenderness, $\lambda = 16$. The brittleness increase by decreasing $s_E$ is obtained as previously, but in this case it is easier to achieve
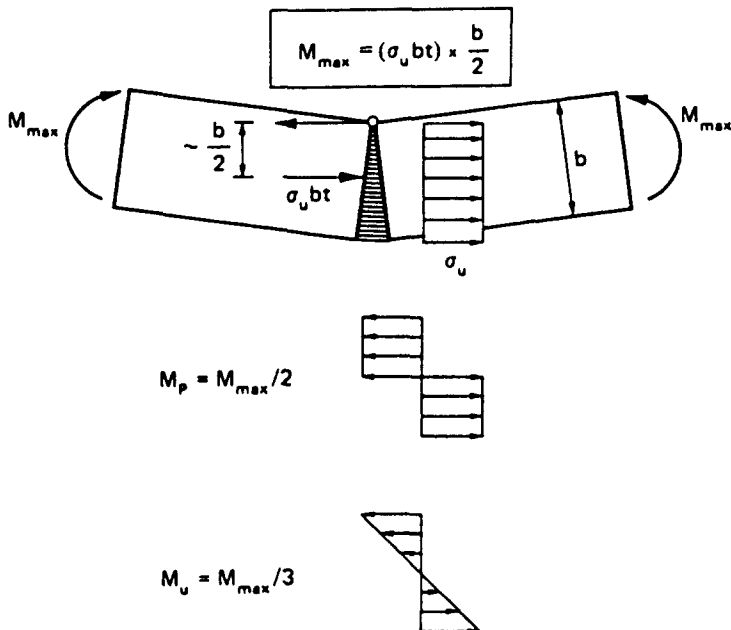


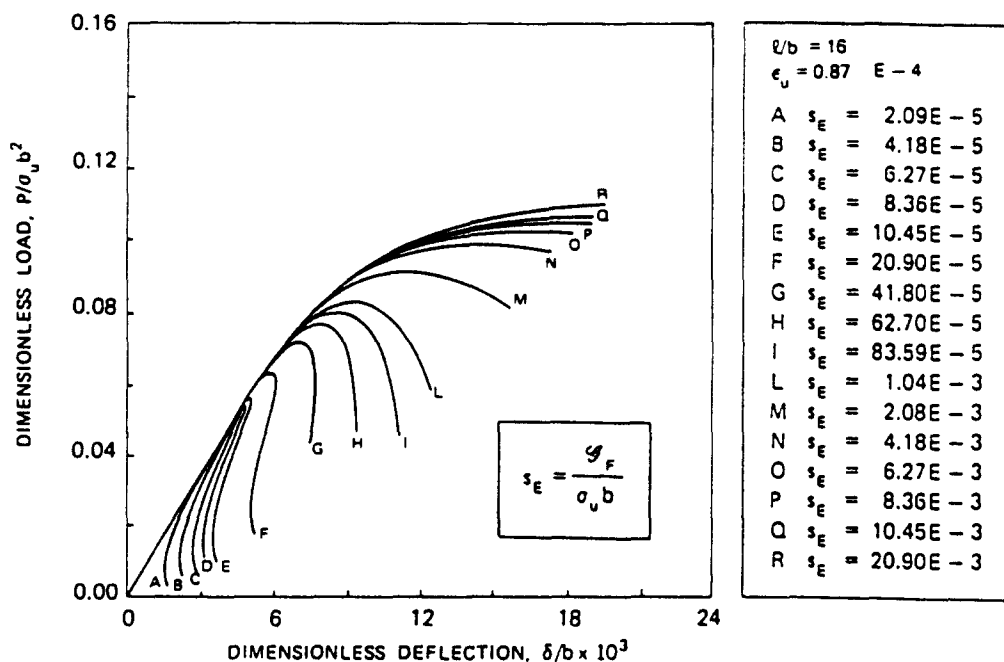Fig. 20. Constant distribution of cohesive stresses.

Fig. 21. Dimensionless load deflection diagrams with various brittleness numbers $s_E = \mathcal{G}_F/\sigma_u b$
($\lambda = 16$, $a_0/b = 0.0$, $\epsilon_u = 0.87 \times 10^{-4}$).

the snap-back instability of the beam when $s_E \leqslant 62.70 \times 10^{-5}$. On the other hand eqn (63) implies that $s_E \leqslant 46.40 \times 10^{-5}$, which is a good approximation.

## 7. CONCLUSIONS

Two different models have been considered:

(1) the ideal material with a random distribution of microdefects (Section 3);

(2) the initially uncracked material with a growing cohesive crack (Section 6).

Both such models lead to a *decrease in the apparent strength* with an increase in the size of the specimen.

In the former idealization, the apparent strength (stress of microcracking initiation) tends to zero when the size tends to infinity, while it tends to the true value $\sigma_u$ (constant material property) when the size tends to zero (Fig. 2(a)).

On the other hand, with the latter model, the apparent ultimate bending strength tends to the true value $\sigma_u$ when the size tends to infinity, whereas it tends to the limit $3\sigma_u$ when the size tends to zero (Figs 19 and 20).

The two models may describe different real situations, according to the geometry and failure mechanism of the specimen. If the microdefects pre-existing in the material produce very severe stress conditions and the failure mechanism is tensile and brittle, the former model is likely to be applicable. On the other hand, if the failure mechanism is stable or ductile and is produced by the slow propagation of a unique crack in a partially compressed material (in bending), the latter model is more suitable for interpreting the ultimate strength decrease with size.

REFERENCES

Barenblatt, G. I. (1959). The formation of equilibrium cracks during brittle fracture. General ideas and hypotheses. Axially symmetric cracks. *J. appl. Math. Mech.* **23**, 622–636.

Bazant, Z. P. (1976). Instability, ductility and size effect in strain-softening concrete. *J. Engng Mech. Div. ASCE* **102**, 331–344.

Bilby, B. A., Cottrell, A. H. and Swinden, K. H. (1963). The spread of plastic yield from a notch. *Proc. R. Soc.* **A272**, 304–314.

Biolzi, L., Cangiano, S., Tognon, G. P. and Carpinteri, A. (in press). Snap-back softening instability in high strength concrete beams. *SEM-RILEM International Conference on Fracture of Concrete and Rock*, Houston (Edited by S. P. Shah and S. E. Swartz).

Carpinteri, A. (1982a). Notch sensitivity in fracture testing of aggregative materials. *Engng Fract. Mech.* **16**, 467–481.

Carpinteri, A. (1982b). Application of fracture mechanics to concrete structures. *J. Struct. Div. ASCE* **108**, 833–848.

Carpinteri, A. (1983). Statistical strength variation in materials with a random distribution of defects. University of Bologna, Istituto di Scienza delle Costruzioni. Internal Report No. 73.

Carpinteri, A. (1985). Interpretation of the Griffith instability as a bifurcation of the global equilibrium. *NATO Advanced Research Workshop on Application of Fracture Mechanics to Cementitious Composites*, Evanston (Illinois) (Edited by S. P. Shah), pp. 287–316. Martinus Nijhoff, Dordrecht.

Carpinteri, A. and Fanelli, M. (1987). Numerical analysis of the catastrophical softening behaviour in brittle structures. *Fourth International Conference on Numerical Methods in Fracture Mechanics*, San Antonio, pp. 369–386. Pineridge Press, Swansea.

Carpinteri, A., Di Tommaso, A. and Viola, E. (1979). Collinear stress effect on the crack branching phenomenon. *Materiaux Constructions* **12**, 439–446.

Di Leonardo, G. (1979). Fracture toughness characterization of materials under multiaxial loading. *Int. J. Fracture* **15**, 537–552.

Dugdale, D. S. (1960). Yielding of steel sheets containing slits. *J. Mech. Phys. Solids* **8**, 100–104.

Fairhurst, C., Hudson, J. A. and Brown, E. T. (1971). Optimizing the control of rock failure in servo-controlled laboratory tests. *Rock Mech.* **3**, 217–224.

Freudenthal, A. M. (1968). Statistical approach to brittle fracture. In *Fracture* (Edited by H. Liebowitz), Vol. II, pp. 591–619. Academic Press, New York.

Hillerborg, A., Modeer, M. and Petersson, P. E. (1976). Analysis of crack formation and crack growth in concrete by means of fracture mechanics and finite elements. *Cement Concrete Res.* **6**, 773–782.

Irwin, G. R. (1957). Analysis of stresses and strains near the end of a crack traversing a plate. *J. appl. Mech.* **24**, 361–364.

Jayatilaka, A. S. (1979). *Fracture of Engineering Brittle Materials*. Applied Science, London.

Leicester, R. H. (1973). Effect of size on the strength of structures. C.S.I.R.O., Forest Products Laboratory, Division of Building Research, Melbourne.

Maier, G. (1968). On the unstable behaviour in elastic-plastic beams in flexure. *Istituto Lombardo, Accademia di Scienze e Lettere, Rendiconti, Classe di Scienze* **A102**, 648–677 (in Italian).

Petersson, P. E. (1981). Crack growth and development of fracture zones in plain concrete and similar materials. Report TVBM 1006, Lund Institute of Technology.

Rice, J. R. (1968). A path independent integral and the approximate analysis of strain concentration by notches and cracks. *J. appl. Mech.* **35**, 379–386.

Rokugo, K., Ohno, S. and Koyanagi, W. (1986). Automatical measuring system of load-displacement curves including post failure region of concrete specimens. International Conference on Fracture Mechanics of Concrete, Lausanne; *Fracture Toughness and Fracture Energy of Concrete* (Edited by F. H. Wittmann), pp. 403–411. Elsevier, Amsterdam.

Sabnis, G. M. and Mirza, S. M. (1979). Size effects in model concretes. *J. Struct. Div. ASCE* **105**, 1007–1020.

Sih, G. C. (1973). *Handbook of Stress-Intensity Factors for Researchers and Engineers*. Institute of Fracture and Solid Mechanics, Bethlehem, PA.

Strange, P. C. and Bryant, A. H. (1979). Experimental tests on concrete fracture. *J. Engng Mech. Div. ASCE* **105**, 337–342.

Walsh, P. F. (1972). Fracture of plain concrete. *Indian Concrete J.* **46**, 469–476.

Weibull, W. (1939). *A Statistical Theory of the Strength of Materials*. Swedish Royal Institute for Engineering Research, Stockholm.

Williams, M. L. (1952). Stress singularities resulting from various boundary conditions in angular corners of plates in extension. *J. appl. Mech.* **19**, 526–528.